2025 IEEE Conference on Antenna Measurements and Applications (CAMA) | 979-8-3315-1508-9/25/$31.00 ©2025 IEEE | DOI: 10.1109/CAMA65664.2025.11335357

Fast Polarimetric Modeling and Calibration of a Multi-Node Antenna Pattern Measurement Setup

1st Máté L. Iványi, 2nd Changxu Zhao, 3rd Yanki Aslan, 4th Alexander Yarovoy, 5th Marco Spirito
Dept. of Microelectronics, Delft University of Tecnhology, Delft, The Netherlands
{M.L.Ivanyi, C.Zhao-2, Y.Aslan, A.Yarovoy, M.Spirito}@tudelft.nl

***Abstract*—To perform the polarimetric calibration of the Antenna Dome – a fixed multi-node over-the-air measurement setup for antenna pattern characterization – a fast simulation model is developed. The model enables characterization and compensation of angle-dependent polarimetric distortions in the transmitted field of an antenna under test (AUT). An open ended waveguide and a horn antenna at 26.5 GHz are used for referencing and validation, respectively. The total power simulated at broadside with the proposed model showed an average power difference of 0.5 dB compared with the measurement results for the reference antenna. The proposed calibration method reduces the power deviation between the full-wave simulation model and the practical Dome measurement system of about 67% in the antenna used for validation. The calibration procedure compensating for systematic power imbalances across the sensing nodes and correcting angle-dependent polarization basis distortions.**

***Index Terms*—antenna measurement, calibration, over-the-air, polarimetry.**

I. Introduction

Over-the-air (OTA) antenna measurements with multi-probe systems offer efficient characterization of antennas [1]. Accurate determination of polarimetric components in antenna patterns is essential to enhance target recognition performance in sensing, and to reduce polarization mismatches in communication via polarimetric calibration. Radar polarimetry has been widely used in weather sensing [2], [3], automotive driving [4]–[6] and defense applications [7], [8]. Dual-polarized antennas have also been widely used in communications for increased capacity [9], [10]. Achieving accuracy in polarimetric pattern measurements remains challenging, particularly at wide scan angles where the polarization basis becomes non-orthogonal [11]. The Antenna Dome [12], developed at TU Delft, is a sparse far-field measurement system equipped with multiple dual-polarized phaseless probes, allowing amplitude-only measurements, which provides a unique test platform for time-efficient polarimetric pattern measurements. Its use in active array diagnostics was recently shown [13].

This work presents, for the first time, a fast simulation framework for the Dome's polarimetric characterization and calibration. The model accounts for geometrical tolerances and variations in received power across sensing nodes, thereby enabling robust compensation of polarimetric distortions. A polarimetric calibration method is proposed and evaluated with the Dome by utilizing an open-ended waveguide antenna as a reference, and a horn antenna for validation.

The remainder of this paper is organized as follows. Section II introduces the Antenna Dome measurement setup and the proposed simulation model in CST Microwave Studio and FEKO. Section III validates the simulation model through comparison with experimental measurements. Section IV presents the polarimetric calibration procedure and demonstrates its effectiveness. Finally, Section V concludes the work.

II. Measurement Setup and Simulation Model

A. Geometry of the Dome

The Antenna Dome is equipped with 36 dual-polarized Vivaldi antennas that act as probes distributed on a geodesic skeleton, as illustrated in Fig. 1. The Dome skeleton has a radius of 1 m. However, to mount the antenna under test (AUT), a holder is placed at the center, raising the AUT. For each AUT, the distance to the broadside node should be measured separately, since the phase center differs for each antenna. The corresponding values are presented later.

The positions of the nodes were determined by measuring the elevation and azimuth angles with a laser mounted on a two-axis Newmark GM-6 gimbal positioner allowing precise rotation in both planes, as illustrated in Fig. 2. The reference angle for each node was set when the laser beam was aligned with the center of the corresponding node board. The gimbal provides an accuracy of $\pm 0.02°$ and a resolution of $0.001°$. The detailed angle values are provided in [14].

Since the distance between the AUT and the broadside node changes for each setup, and is also different for the rotation center of the gimbal, the elevation cut for each transmitted radiation pattern must be recalculated for every configuration. This concept is illustrated in Fig. 3, from which the corrected elevation angle for the ith node can be calculated as

$$\vartheta_{2,i} = atan\left(\frac{sin(\vartheta_{1,i})h_1}{cos(\vartheta_{1,i})h_1 - (h_1 - h_2)}\right) \qquad (1)$$

where $\vartheta_{1,i}$ is the initial measured elevation angle of the ith node, corresponding to the angles given in [14] for the reference distance of $h_1 = 1$ m. For comparison, $h_2 = 0.67$ m is the distance between the open-ended waveguide AUT aperture and the broadside node in our setup.

B. Dual-Polarized Sensing Nodes

Each sensing node integrates two orthogonally oriented Vivaldi antennas, with polarization components corresponding

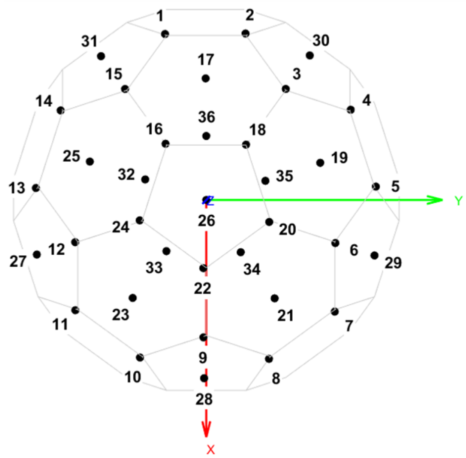

Fig. 1. Top view illustration of the Antenna Dome structure, showing the node positions as black dots labeled with numbers.

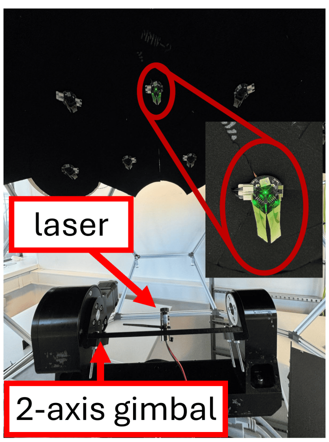

Fig. 2. Illustration of the laser setup used for angle measurements.

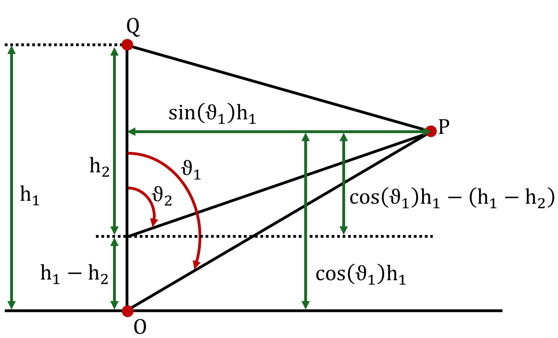

Fig. 3. Illustration of the method for calculating the elevation angle of each node based on the distance between the broadside node and the AUT. Here, ϑ_1 denotes the initial elevation angle of the ith node, ϑ_2 the current elevation angle, h_1 the reference distance, and h_2 the current distance between the AUT and the broadside node.

to $+45°$ and $-45°$ (Fig. 4), indicated by the green and blue arrows, respectively. These orientations are defined with respect to the reference axis shown as the dotted line in the figure.

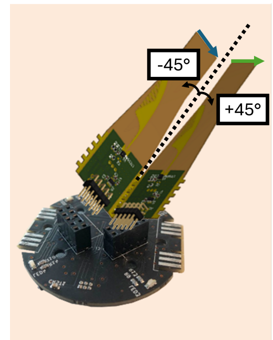

Fig. 4. Dual-polarized sensing node (the green and the blue arrows indicate the +45° pol and -45° pol, respectively).

C. Simulation Model

In the proposed simulation model, the far-field radiation patterns of both the probes and the AUT were obtained in CST Microwave Studio, as shown in Fig. 5 and Fig. 6. These far-field radiation patterns were then imported into FEKO and assigned to the source and receivers, as illustrated in Fig. 7.

In the simulation model, coupling effects – both between different probes and between the two polarizations of a single probe – are neglected, since the relatively large distances between probes and the low cross-polarization levels of the Vivaldi antennas (see Fig. 6(c)) suggest minimal interaction. However, this assumption may be less accurate under unequal power illumination (e.g., in the case of a directive AUT), where certain probes could scatter more strongly and influence neighboring probes. The model is thus intentionally idealized in this respect, making it suitable as a reference for calibrating the real measurement setup. Consequently, it is sufficient to create two separate models: one comprising all $+45°$ polarized antennas and the other all $-45°$ polarized antennas, without coupling effects between nodes, thereby reducing the runtime.

To verify this assumption, the far-field radiation pattern of a dual-polarized sensing node, consisting of two orthogonal Vivaldi antennas, was simulated in CST. As shown in Fig. 8, the coupling between the orthogonal antennas has a negligible effect on the polarimetric results. In addition, the total pattern, defined as the sum of the two polarization components, shows good agreement with the AUT source pattern obtained from CST, thereby validating the accuracy of the model.

To capture the polarimetric components at each node, the AUT, represented by a WR-28 open-ended waveguide, was placed beneath the Dome and rotated in azimuth by 360°. Each probe was oriented using the measured elevation and azimuth angles.

In most full-wave simulation software, such as the CST Microwave Studio, the radiation pattern is often defined with the source located at the origin. In the physical system, and thus in the FEKO model, however, the AUT must be mounted on holders, which, as mentioned earlier, raise it above the initial reference point. As a result, the AUT moves closer to the broadside node, while the effective elevation angles of all other nodes increase. To obtain the correct elevation angles in CST, an elevation cut corresponding to the actual AUT height relative to the broadside node must be identified as illustrated in Fig. 3.

The effect of polarization-basis distortion of the transmitted wave can be observed in the off-broadside pattern simulations. At broadside, the polarization basis of the source remains undistorted, resulting in a 90° separation between the adjacent maxima of the two polarization curves. This aligns with previous broadside measurements [12]. However, at the $\vartheta_1 = 64.1°$ off-broadside node, distortion in the transmitted polarization basis reduces the peak separation to $40°$ (see Fig. 8(d)).

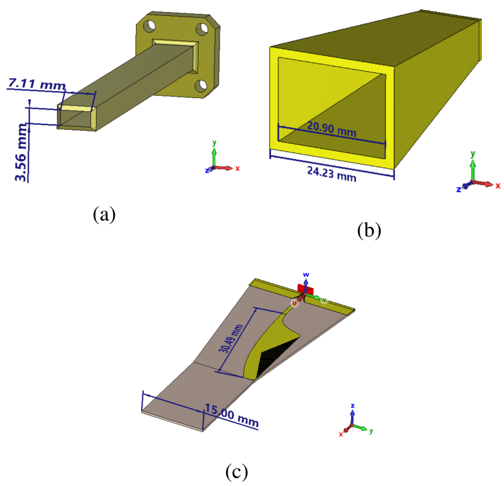

Fig. 5. Perspective view of the CST models of the (a) open-ended waveguide, (b) horn and (c) Vivaldi antennas.

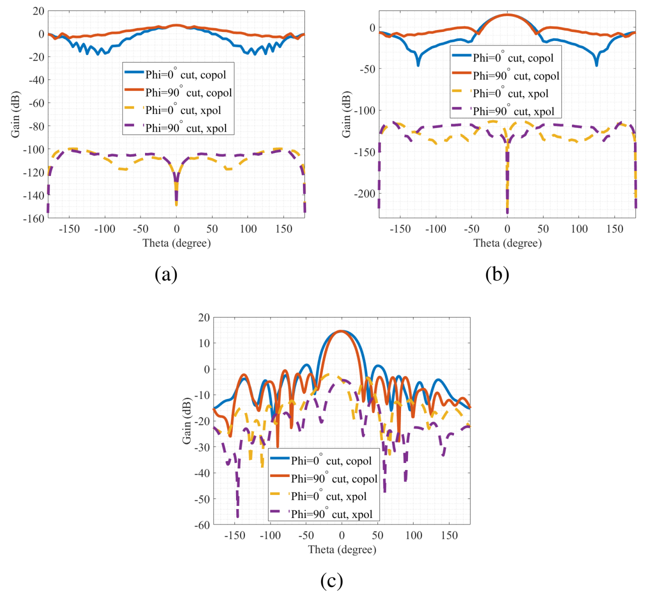

Fig. 6. Far-field radiation pattern cuts of the (a) open-ended waveguide, (b) horn and (c) Vivaldi antennas, simulated in CST.

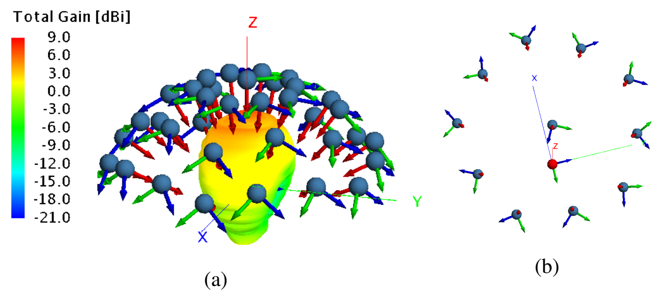

Fig. 7. The proposed simulation setup for the Antenna Dome in FEKO: (a) perspective view with the pattern of the AUT; (b) bottom view of the broadside node and the first surrounding ring. The green and the blue arrows indicate the $+45°$ pol and $-45°$, respectively, while the AUT is shown in red at the origin.

III. Validation of the Simulation Model with Measurements

To validate the model, the two orthogonal polarization components were compared with measurement data. In the measurement setup, the WR-28 open-ended waveguide serving as the AUT was mounted on a 2-axis gimbal to enable full rotation, as shown in Fig. 9. The distance between the AUT and the broadside node was 0.67 m. The Dome was fully covered with absorbers to suppress multiple reflections from the ground and the skeleton, and prevent degradation of the received power. The results from the broadside node show strong agreement between measured and simulated polarimetric patterns (Fig. 10), with an average power deviation of the total power around 0.5 dB, confirming the accuracy of the model. The ripples observed in the measured total power at broadside result from positioning errors of the AUT. For the off-broadside nodes, deviations between the measurements and simulations can be observed. These are mainly caused by systematic errors in the measurement system, including mechanical tolerances of the Dome skeleton, probe positioning errors, fluctuations in probe responses, and polarimetric distortion.

IV. Calibration of the Measurement Setup

The simulation model proposed has been used for polarimetric calibration of the Antenna Dome. The reference antenna employed was an open-ended waveguide, which provides a wide radiation pattern suitable for calibrating all nodes inside the Dome. For validation of the proposed approach, a WR-28 horn antenna is used. The distance between the horn antenna and the broadside node was 0.73 m. Due to its narrower radiation pattern, the test with the horn is limited to the near-broadside nodes, namely the broadside node and the first surrounding ring. Calibration of the remaining nodes can be achieved with larger transmit power, a validation source

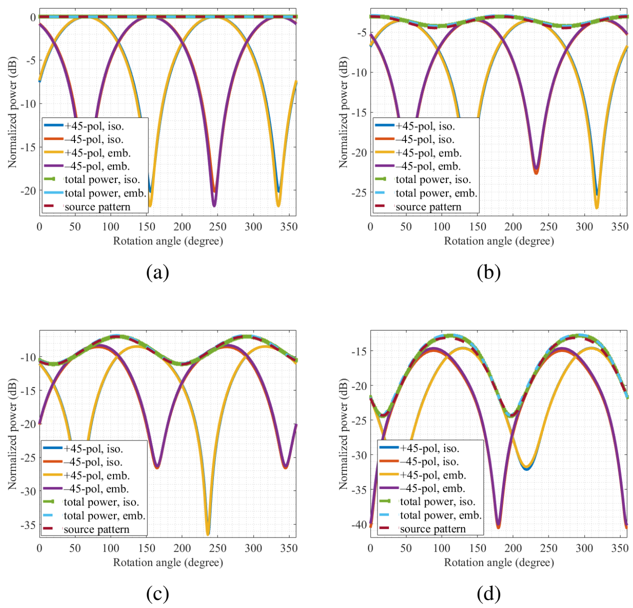

Fig. 8. Comparison of the polarimetric responses of four nodes in the proposed simulation model, with and without coupling between the dual-polarized probes, together with the total pattern and the source pattern obtained from CST: (a) Node 26 at $\vartheta_1 = \vartheta_2 = 0°$; (b) Node 22 at $\vartheta = 20.2°$ and $\vartheta_2 = 30°$; (c) Node 25 at $\vartheta = 38.5°$ and $\vartheta_2 = 54°$; and (d) Node 29 at $\vartheta = 64.1°$ and $\vartheta_2 = 83°$. The distance between the AUT and the broadside node was h=0.67 m.

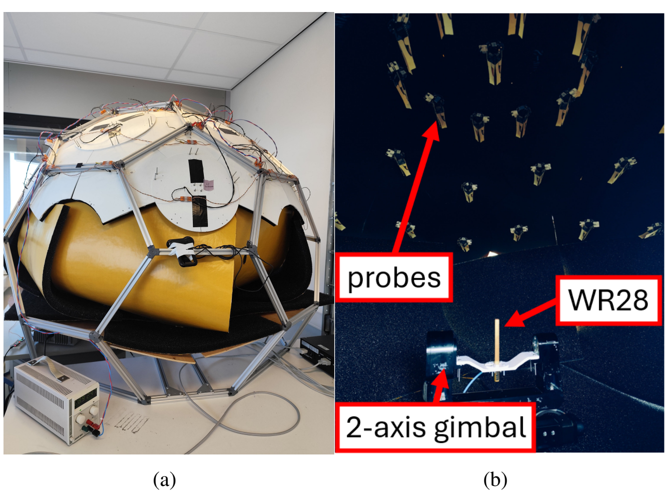

Fig. 9. Measurement setup with the Antenna Dome for polarimetric power pattern measurements: (a) outside of the Dome, fully covered by absorbers; (b) inside of the Dome (the WR-28 open-ended waveguide antenna was rotated from 0° to 360° using the gimbal in order to obtain the full polarimetric response of the dual-polarized nodes).

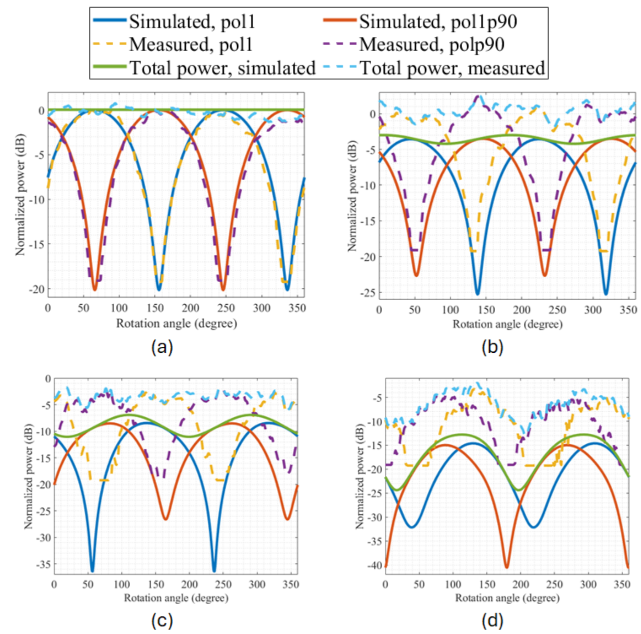

Fig. 10. Comparison of the polarimetric responses together with the total pattern of four nodes in the Antenna Dome measurement setup and the proposed simulation model: (a) Node 26 at $\vartheta = 0°$; (b) Node 22 at $\vartheta = 20.2°$; (c) Node 25 at $\vartheta = 38.5°$; and (d) Node 29 at $\vartheta = 64.1°$. The distance between the AUT and the broadside node was $h_2 = 0.67$ m.

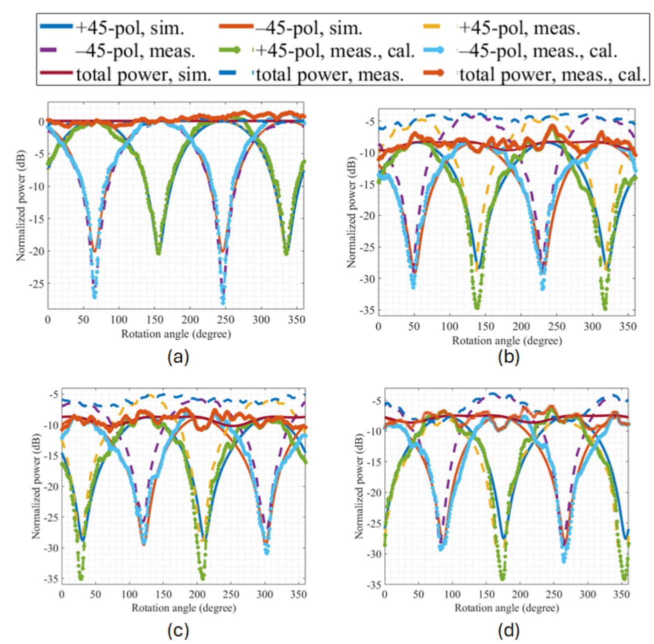

Fig. 11. Comparison of the polarimetric responses together with the total pattern of four nodes in the Antenna Dome measurement setup and the proposed simulation model: (a) Node 26 at $\vartheta = 0°$; (b) Node 22 at $\vartheta = 20.2°$; (c) Node 24 at $\vartheta = 20.75°$; and (d) Node 33 at $\vartheta = 19.2°$. The distance between the AUT and the broadside node was $h_2 = 0.73$ m.

that provides a wider beam, or with a phased array having wide-angle scanning capabilities.

The calibration coefficient for each node is determined from the power difference between the simulated and measured patterns obtained with the open-ended waveguide, computed separately for each polarization and rotation angle at each node of interest. For the horn measurements, this calibration coefficients are applied to the measured results. Fig. 11. shows the horn measurement results before and after calibration, together with the corresponding FEKO simulation as the reference. As observed, the calibrated measurements show significantly improved agreement with the simulations. For each node, the mean power difference between the measurements and the simulations was calculated across all rotation angles. Considering the nodes on the first ring, the average of these mean differences decreased from 3 dB to 0.98 dB – an improvement of approximately 67%, – while the maximum decreased from 4.37 dB to 1.46 dB and the minimum from 1.69 dB to 0.7 dB, thereby confirming both the accuracy of the model and the effectiveness of the proposed polarimetric calibration approach for the Antenna Dome.

V. Conclusion

A novel rapid simulation model, tailored to the fixed multi-node over-the-air measurement system known as the Antenna Dome is proposed. The model enables efficient characterization and compensation of angle-dependent polarimetric pattern distortions. The accuracy of the model was verified with full-wave simulations. Subsequently, measurements with the Antenna Dome at 26.5 GHz utilizing an open ended waveguide with a 2-axis gimbal were performed to validate the model, yielding an average power difference of 0.5 dB between the model and measurements at the broadside node. Dome system calibration has been performed at each node and rotation angle, which reduces the average power deviation by about 67% for the horn-type AUT.

References

[1] L. J. Foged, G. Barone, and F. Saccardi, ”Antenna measurement systems using multi-probe technology,” in *Proc. IEEE CAMA*, Chiang Mai, Thailand, 2015, pp. 1–3.

[2] R. D. Palmer, M. B. Yeary, D. Schvartzman, J. L. Salazar-Cerreno, C. Fulton, M. McCord, B. Cheong, D. Bodine, P. Kirstetter, H. H. Sigmarsson, T.-Y. Yu, D. Zrnić, R. Kelley, J. Meier, and M. Herndon, ”Horus—A fully digital polarimetric phased array radar for next-generation weather observations,” *IEEE Trans. Radar Syst.*, vol. 1, pp. 96–117, 2023.

[3] G. Zhang, R. J. Doviak, D. S. Zrnic, J. Crain, D. Staiman, and Y. Al-Rashid, ”Phased array radar polarimetry for weather sensing: A theoretical formulation for bias corrections,” *IEEE Trans. Geosci. Remote Sens.*, vol. 47, no. 11, pp. 3679–3689, Nov. 2009.

[4] A. Tinti, S. Tejero Alfageme, S. Duque Biarge, J. Balcells-Ventura, and N. Pohl, ”Fully polarimetric automotive radar: Proof of concept,” *IEEE Trans. Radar Syst.*, vol. 2, pp. 645–660, 2024.

[5] W. Bouwmeester, F. Fioranelli, and A. Yarovoy, ”Statistical modeling of polarimetric RCS of road surfaces for scattering simulation and optimal antenna polarization determination,” *IEEE J. Sel. Topics Appl. Earth Observ. Remote Sens.*, vol. 17, 2024.

[6] C. Zhao, A. Garcia-Tejero, W. Bouwmeester, Y. Aslan, O. Krasnov, and A. Yarovoy, ”Calibration of polarimetric automotive radar with asymmetric MIMO topology and off-broadside beamforming,” in *Proc. Eur. Radar Conf. (EuRAD)*, 2024, pp. 87–90.

[7] H. V. Sethuraman, A. Yarovoy, and F. Fioranelli, ”Classification of unmanned aerial vehicles (UAVs) carrying payloads with polarimetric radar,” in *Proc. Eur. Radar Conf. (EuRAD)*, 2021, pp. 365–368.

[8] A. Lupidi, C. Greiff, S. Brüggenwirth, M. Brandfass, and M. Martorella, ”Polarimetric radar technology for European defence superiority—The PolRad project,” in *Proc. Int. Radar Symp. (IRS)*, 2020, pp. 6–10.

[9] Wu, S., Feng, B., Ding, X., Sun, S., Deng, L., & Zeng, Q. ”Design of a Wideband Dual-Polarized Antenna for 2G/3G/LTE/5G Base Station.” in *2023 IEEE 6th International Conference on Electronic Information and Communication Technology (ICEICT)*, 607–608.

[10] Yin, J., Jia, Y., Yang, S., & Zhai, H. (2022). “Design of a Composite Decoupling Structure for Dual-Band Dual-Polarized Base Station Array.” in *IEEE Antennas and Wireless Propagation Letters*, 21(7), 1408–1412.

[11] C. Zhao, Y. Aslan, and A. Yarovoy, ”Overview of polarimetry in application to automotive radar: Array design, calibration and target feature extraction concepts,” in *Proc. Eur. Conf. Antennas Propag. (EuCAP)*, Stockholm, Sweden, 2025, pp. 1–5.

[12] R. A. Coesoij, et al., ”Calibration approaches in multi-node antenna characterization setups,” in *Proc. ARFTG Conf.*, Las Vegas, NV, USA, 2023, pp. 1–4.

[13] A. Kannan, N. B. Onat, M. S. A. Yarovoy and Y. Aslan, ”Detection of Faulty Elements From Sparse Far-Field Data in Active Phased Arrays via Machine Learning,” in *IEEE Open Journal of Antennas and Propagation*, 2025, pp. 1-11.

[14] Iványi, Máté; Zhao, Changxu; Aslan, Yanki (2025), ”Measured Azimuth and Elevation Angles of the Antenna Dome Sensing Nodes.” Version 1. *4TU.ResearchData*. dataset. https://doi.org/10.4121/4223e398-952b-413d-a329-72c2c10946fa.v1